

# Journal of Biomedical Optics

BiomedicalOptics.SPIEDigitalLibrary.org

## Combination of virtual point detector concept and fluence compensation in acoustic resolution photoacoustic microscopy

Valeriya V. Perekatova  
Mikhail Yu. Kirillin  
Ilya V. Turchin  
Pavel V. Subochev

**SPIE.**

Valeriya V. Perekatova, Mikhail Yu. Kirillin, Ilya V. Turchin, Pavel V. Subochev, "Combination of virtual point detector concept and fluence compensation in acoustic resolution photoacoustic microscopy," *J. Biomed. Opt.* **23**(9), 091414 (2018), doi: 10.1117/1.JBO.23.9.091414.

# Combination of virtual point detector concept and fluence compensation in acoustic resolution photoacoustic microscopy

Valeriya V. Perekatova,\* Mikhail Yu. Kirillin, Ilya V. Turchin, and Pavel V. Subochev

Russian Academy of Sciences, Institute of Applied Physics, Nizhny Novgorod, Russia

**Abstract.** We propose a hybrid approach to image enhancement in acoustic resolution photoacoustic microscopy. The developed technique is based on compensation for nonuniform spatial sensitivity of the optoacoustic (OA) system in both optical and acoustic domains. Spatial distribution of optical fluence is derived from full three-dimensional Monte Carlo simulations accounting for conical geometry of tissue laser illumination at the wavelength of 532 nm. Approximate nonuniform spatial response of acoustic detector with numerical aperture of 0.6 is derived from the two-dimensional k-Wave modeling. Application of the developed technique allows to improve the spatial resolution and to balance in-depth signal-level distribution in OA images of phantom and *in-vivo* objects. © 2018 Society of Photo-Optical Instrumentation Engineers (SPIE) [DOI: 10.1117/1.JBO.23.9.091414]

Keywords: optoacoustic imaging; synthetic aperture focusing technique; antenna spatial response; fluence compensation; Monte Carlo simulations.

Paper 180091SSRR received Feb. 12, 2018; accepted for publication Jul. 13, 2018; published online Jul. 31, 2018.

## 1 Introduction

Biomedical optoacoustic (or photoacoustic) (OA) imaging is based on wideband detection of ultrasonic waves generated by the tissue chromophores absorbing probing laser pulses of nanosecond duration. One of the simplest hardware implementations of three-dimensional (3-D) OA imaging is acoustic resolution photoacoustic microscopy (AR-PAM) based on raster-scanning of the studied object by spherically focused ultrasonic detector with high bandwidth and numerical aperture (NA) defining the spatial resolution;<sup>1</sup> however, higher NAs of acoustic detection decrease AR-PAM depth of field. To improve resolution of 3-D AR-PAM imaging in the out-of-focus area, a studied sample can be scanned in additional focal planes;<sup>2</sup> model-based algorithms of acoustic inversion<sup>3</sup> are also beneficial.

One of the most common algorithms of acoustic inversion is synthetic aperture focusing technique (SAFT), which is often applied in conventional ultrasound imaging.<sup>4-6</sup> The first successful application of SAFT in OA imaging was reported in Ref. 7 for point-like detectors. Virtual-point-detector (VPD) concept<sup>1</sup> allowed to apply two-dimensional (2-D) SAFT algorithms for AR-PAM imaging with spherically focused detectors of high NA. In Ref. 8, 2-D SAFT was applied for two perpendicular cross sections, thus providing an isotropic lateral resolution at AR-PAM images. Further improvement in the lateral resolution of AR-PAM was shown in work<sup>9</sup> by applying adaptive 2-D SAFT in one of the two cross sections depending on spatial orientation of the reconstructed blood vessels. Nevertheless, quasi-3-D implementations<sup>8,9</sup> of the SAFT technique<sup>1</sup> applied to 3-D AR-PAM datasets came at a cost of artifacts provided by the signals along the third, unaccounted, dimension; however, full 3-D implementations of SAFT technique recently reported in Refs. 10 and 11 can lead to the artifacts associated with the object's motion.<sup>12</sup>

Although conventional implementations of SAFT<sup>1,8,9</sup> allowed significant improvement in the lateral resolution above and below VPD depth, they all suffered from the decreased SNR at VPD depth. To increase SNR weighting, coefficients corresponding to spatial impulse response of the ultrasonic detector were introduced to SAFT.<sup>10</sup> Combination of SAFT with 3-D deconvolution<sup>11</sup> also allowed efficient suppression of VPD artifacts while providing an additional improvement of axial resolution in reconstructed AR-PAM images.

Serious limitation of AR-PAM 3-D imaging is a rapid in-depth attenuation of probing laser radiation due to strong scattering and absorption in biological tissues. For example, at the wavelength of 532 nm often employed for AR-PAM angiography, the effective optical attenuation coefficient of biotissue is of the order of  $1 \text{ mm}^{-1}$ . Although SAFT algorithms<sup>1,8-11</sup> were based on the assumption of homogeneous illumination, a universal weighted SAFT accounting for incident beam properties, and optical properties of the imaged object was recently proposed.<sup>13</sup> Meanwhile, the optical illumination system of AR-PAM usually employs conical laser-beam geometry aiming for confocal probing. Accurate calculation of fluence distribution within sample produced by such beams can hardly be achieved by analytical techniques,<sup>13</sup> especially if the sample is optically inhomogeneous. In this situation, Monte Carlo simulation of light transport accounting for complex geometry of laser illumination seems to be an optimal tool.<sup>14</sup>

In this paper, we report a reconstruction algorithm comprising improved SAFT algorithm<sup>1,11,15,16</sup> accounting for both the spatial response<sup>17</sup> of the acoustic antenna<sup>10</sup> and the spatial distribution of optical fluence.<sup>14,18</sup> For precise calculation of rapid in-depth attenuation of probing laser radiation, we employ 3-D Monte Carlo code previously customized for simulation of the complex geometry of AR-PAM light illumination in medium with optical properties typical for biotissues.<sup>14</sup> At the first

\*Address all correspondence to: Valeriya V. Perekatova, E-mail: ValeriyaPerekatova@gmail.com

step, the SAFT procedure with account for antenna spatial response (ASR) is performed. Accurate account for the ASR is considered along with the proposed simplified approach allowing for significant speedup in processing. At the second step, each A-scan from the reconstructed AR-PAM data is compensated for the calculated in-depth fluence profile at the detector axis. AR-PAM with developed technique was employed for both phantom objects and *in-vivo* imaging demonstrating enhancement of image quality.

## 2 Materials and Methods

### 2.1 Combination of Fluence Compensation and SAFT Accounting for Spatial Response of Acoustic Antenna

The proposed complementary approach includes previously developed fluence compensation technique accounting for complex illumination geometry<sup>14</sup> and SAFT technique additionally accounting for the spatial response of the acoustic antenna. The ASR was derived from the method proposed in Ref. 19 consisting in calculation of point spread function of acoustic antenna using the k-Wave MATLAB Toolbox software.<sup>20</sup>

The first step is the acoustic reconstruction by SAFT. In conventional SAFT, the focal point of the ultrasonic transducer is treated as a VPD. The conventional VPD-based SAFT consists in calculation of appropriate signal delays<sup>1</sup> relative to the VPD for the adjacent scan lines and then summation of the delayed signals. We employed SAFT to produce reconstructed image in 2-D realization [Fig. 1(b)] as

$$Bscan^{rec}(x_s, z_s) = \sum_{x_f} Bscan^{raw}[x_f, z_f + sgn(z_s - z_f)] \cdot \sqrt{(z_s - z_f)^2 + (x_s - x_f)^2}, \quad (1)$$

or in full 3-D realization [Fig. 1(a)]

$$Bscan^{rec}(x_s, y_s, z_s) = \sum_{\vec{r}_d} Bscan^{raw} \left[ \vec{r}_d, z_f + sgn(z_s - z_f) \cdot \sqrt{(z_s - z_f)^2 + (r_d)^2} \right], \quad (2)$$

where  $Bscan^{raw}$  is the raw OA B-scan,  $Bscan^{rec}$  is the reconstructed OA B-scan,  $(x_s, y_s, z_s)$  are the coordinates of the reconstructed image,  $(x_s, y_s, z_s)$  are the coordinates of focus,  $r_d$  is the distance from the focal point to the projection of the “true” source to the focal plane,  $sgn(z_s - z_f)$  is the sign function,  $z_s > z_f$  corresponds to the sources located under the focal point, and  $z_s < z_f$  corresponds to the sources located above the focal point. For the OA source located in the focus ( $z_s = z_f$ ), the raw signal is not modified and is preserved in accordance with the raw data.<sup>10,11</sup>

However, the signal from the source located apart from the A-scan axis (Z-axis) will be detected only if the source is located within the ASR map, and this condition should be implemented in the SAFT algorithm.

Similar to Ref. 10, we multiplied each A-scan line of a raw B-scan to a weighting mask of ASR corresponding to the detector current position. As 2-D SAFT is applied to each B-scan, we performed calculations of the ASR map<sup>19</sup> using the k-Wave toolbox in 2-D computational grid to reduce calculation time. The modeling was performed for the spatial-temporal grid (7.75 by 10.7 mm) × (8.8 μs) with the steps  $\Delta x = \Delta z = 50 \mu m$  and  $\Delta t = 10$  ns. The maximum frequency of the signal that can be detected by the antenna was equal to 15 MHz. We modeled OA signals from a point source recorded by the arc with the focal distance  $R = 6.7$  mm and the aperture  $a = 5$  mm, which corresponds to our spherically focused detector [Fig. 1(b)].

In 2-D computational grid for the current position  $x_f$  of the detector, we placed a point source at the positions  $(x_s, z_s)$  and registered a signal from this source at the detector represented by the arch [Fig. 1(b)]. Figure 2(a) shows impulse responses of

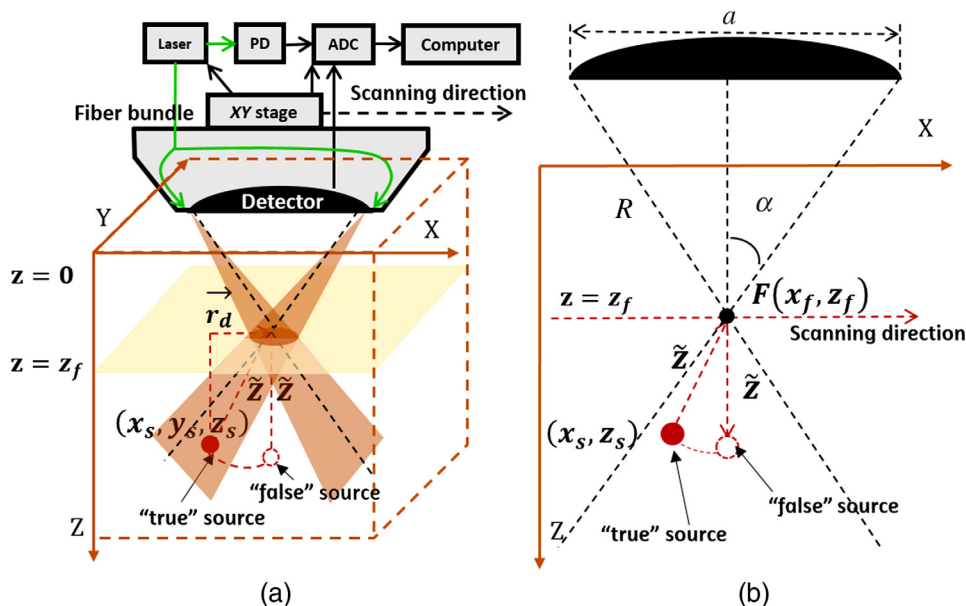


**Fig. 1** (a) Schematic of AR-PAM system, geometry of the scanning head, and 3-D SAFT and (b) schematic of 2-D SAFT.

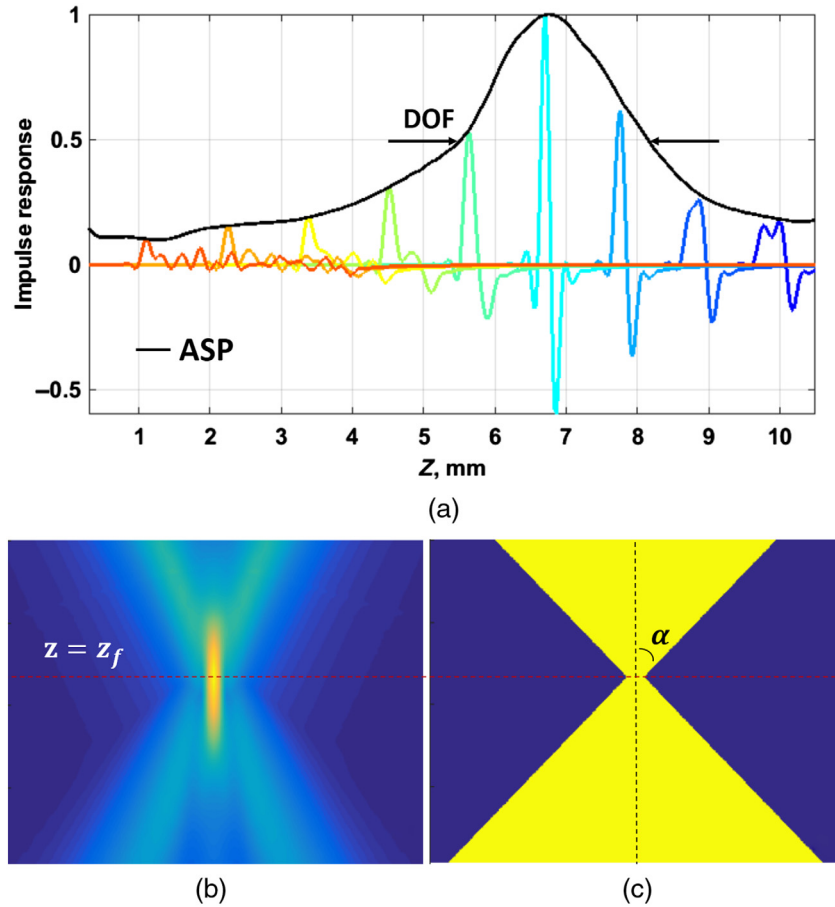


**Fig. 2** (a) Impulse responses of acoustic detector (different colors represent different source depths) and ASP (black line) calculated as maxima of impulse responses, (b) matrix of ASR for current position of the detector, and (c) schematic of detection cone mask for the spherically focused acoustic detector.

acoustic detector from point sources located at different depths below and above the focal positions  $(x_f, z_s)$ .

The ASR  $(x_f, x_s, z_s)$  matrix was formed from maxima of OA impulse responses obtained from the corresponding points  $(x_f, x_s, z_s)$ . Therefore, the ASR matrix is formed only as the amplitude matrix. The resultant ASR for the current detector position is shown in Fig. 2(b). We applied modified 2-D SAFT technique with ASR weighting to *B*-scans as

$$Bscan^{rec}(x_s, z_s) = \sum_{x_f} Bscan^{raw}[x_f, z_f + sgn(z_s - z_f) \cdot \tilde{z}] \otimes ASR[x_f, x_s, z_f + sgn(z_s - z_f) \cdot \tilde{z}], \quad (3)$$

where  $\tilde{z} = \sqrt{(z_s - z_f)^2 + (x_s - x_f)^2}$  is the distance from the focal point to the reconstruction point [Fig. 1(b)] and “ $\otimes$ ” stands for element-wise multiplication of matrices.

As accounting for ASR in SAFT has been implemented in a matrix form [Eq. (3)], its drawback is the large computational time. To overcome this limitation, accounting for ASR was substituted to combination of two procedures: applying a detection cone binary mask (DCM) corresponding to the geometrical shape of ASR [Fig. 2(c)] and image normalization in accordance with the axial sensitivity profile (ASP) of antenna [Fig. 2(a) (black line)]. Both these characteristics were taken from the

simulated ASR [Fig. 2(b)]: the DCM is determined by the angular aperture  $[2\alpha$  in Fig. 1(b)] of the acoustic antenna and the waist of ASR in the focal plane, whereas the ASP is the *z*-profile of ASR at the detector axis. Thus, the binary mask (DCM) is an additional part that allows into account only for the most principal points. The decrease in the number of summation points leads to significant reduction in the computation time.

The second step of the reconstruction is the fluence compensation technique consisting in normalization of the reconstructed OA signal in a given point for the value of local fluence in this point. To produce this compensation, each *A*-scan of the resulting 3-D OA image is normalized by one-dimensional (1-D) array of effective fluence distribution derived from full 3-D Monte Carlo simulation with optical parameters close to those of imaged biotissue accounting for the geometry of complex optical illumination [Fig. 1(a)].

To compare conventional 2-D SAFT reconstruction with the proposed methods, we introduced image contrast as

$$Contrast = 10 \log_{10} \left[ \frac{\iint_{\sigma} Bscan(x_s, z_s) d\sigma}{\iint_{\Sigma} Bscan(x_s, z_s) d\sigma} \right], \quad (4)$$

the ratio of the OA signal intensities integrated over the main source peak area  $\sigma$  and over the area containing surrounding artifacts  $\Sigma$ .

## 2.2 Phantom and In-Vivo Studies

In Fig. 1(a), the block diagram of the AR-PAM system for *in-vivo* imaging<sup>21</sup> is presented. The geometrical configuration of scanning OA head provides confocal laser illumination and ultrasonic detection [Fig. 1(a)]. The illumination fiber bundle consists of 77 optical fibers with 100- $\mu\text{m}$  core diameter and 0.12 NA: 70 of them are oriented at 37 deg to the Z-axis and 7 are used for beam sampling. A custom-made spherically focused PVDF detector with 35-MHz central frequency, 30-MHz bandwidth,  $F = 6.7\text{-mm}$  focal distance, and 0.6 NA provides 50- $\mu\text{m}$  lateral resolution in the focal area in phantom experiments.

In all phantom and *in-vivo* experiments, we used Wedge HB 532 (BrightSolutions, Italy) laser providing 1-ns laser pulses at 532-nm wavelength with the repetition rate of 2 kHz. Each laser pulse (illuminates the medium at a fixed position of OA head along the X- and Y-axes) produces simultaneously US and OA A-scans, respectively.<sup>22</sup> As a result of continuous scanning, A-scans corresponding to discrete XY positions of the scanning head were acquired by 200-MHz 16-bit analog-to-digital converter Razor16 (GaGe) and formed 3-D OA image.

All model experiments were performed with a phantom consisted of 14 copper wires with diameter of 30  $\mu\text{m}$  embedded in a 2% water solution of Lipofundin. The OA B-scans of the phantom were obtained by mechanical scanning within a 7-mm area in the X-direction with lateral scanning step of 5  $\mu\text{m}$ , resulting in a B-scan consisting of 1400 A-scans. The phantom images were acquired for focus position  $z_f = 1.7\text{ mm}$  under the surface.

**Table 1** Optical properties of phantom and skin *in vivo* at the wavelength of 532 nm.

	Skin phantom	Skin <i>in vivo</i>
$\mu_a, \text{mm}^{-1}$	0.057	0.3
$\mu_s, \text{mm}^{-1}$	5.37	10
$g$	0.631	0.8
$z_f, \text{mm}$	1.7	1.5

Lateral scanning step of 25  $\mu\text{m}$  was used for all *in-vivo* experiments. All the images were obtained for focus position  $z_f = 1.5\text{ mm}$  in the Z-direction. After acquisition, the raw data were interpolated to achieve a transversal step of 5  $\mu\text{m}$  with further high-pass filtration. All *in-vivo* experiments were conducted with Caucasian skin of human palm of a healthy female volunteer aged 24 from the research team.

## 2.3 Monte Carlo Simulation of Optical Fluence

To simulate fluence distribution provided by the ring-shaped illumination of the AR-PAM system, previously developed full 3-D Monte Carlo code that is allowed to account for the exact geometry of the probing beam<sup>14</sup> is used. The simulation produces in-depth fluence distribution at the detector axis. The optical parameters of the phantom are obtained from spectrophotometry measurements with a Analytik Jena Specord 250 Plus (Germany) system and properties of skin *in vivo* are taken as typical for human skin.<sup>23,24</sup> The input values in Monte Carlo code are shown in Table 1.

The simulations of fluence distribution were performed for focus position at 1.5 mm under the object surface for *in-vivo* experiments and at 1.7 mm under the surface for phantom experiments. The results of Monte Carlo simulated fluence profiles for phantom (red line) and skin *in vivo* (blue line) studies are shown in Fig. 3(a).

To demonstrate the comparison of the fluence correction for traditional exponential dependence and the proposed Monte Carlo derived fluence distribution with accounting for the complex illumination geometry, we performed Monte Carlo simulations for two different focus positions:  $z_f = 0\text{ mm}$  [Fig. 3(b)

**Table 2** Optical properties used for Monte Carlo modeling for phantom measurements.

	Case 1	Case 2	Case 3	Case 4	Case 5
$\mu_a, \text{mm}^{-1}$	<b>0.057</b>	0.0285	0.114	0.057	0.057
$\mu_s, \text{mm}^{-1}$	<b>5.37</b>	5.37	5.37	2.685	10.74
$g$	<b>0.631</b>	0.631	0.631	0.631	0.631

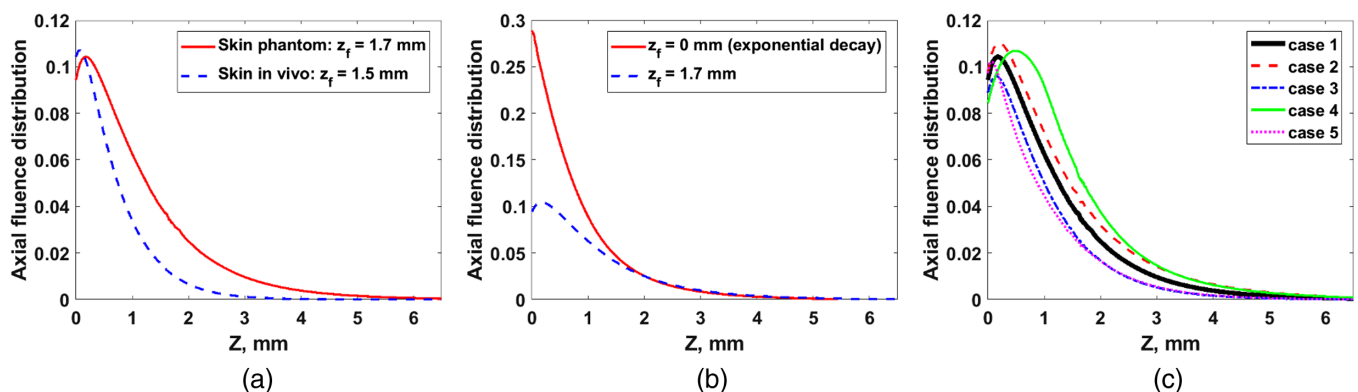


**Fig. 3** Monte Carlo simulated in-depth distribution of optical fluence normalized by the number of launched photons: (a) for skin phantom ( $z_f = 1.7\text{ mm}$ ) (red line) and skin *in vivo* ( $z_f = 1.5\text{ mm}$ ) (blue line), (b) for different focus positions in phantom:  $z_f = 0\text{ mm}$  (red line);  $z_f = 1.7\text{ mm}$  (blue line), and (c) for varied phantom optical properties shown in Table 2.

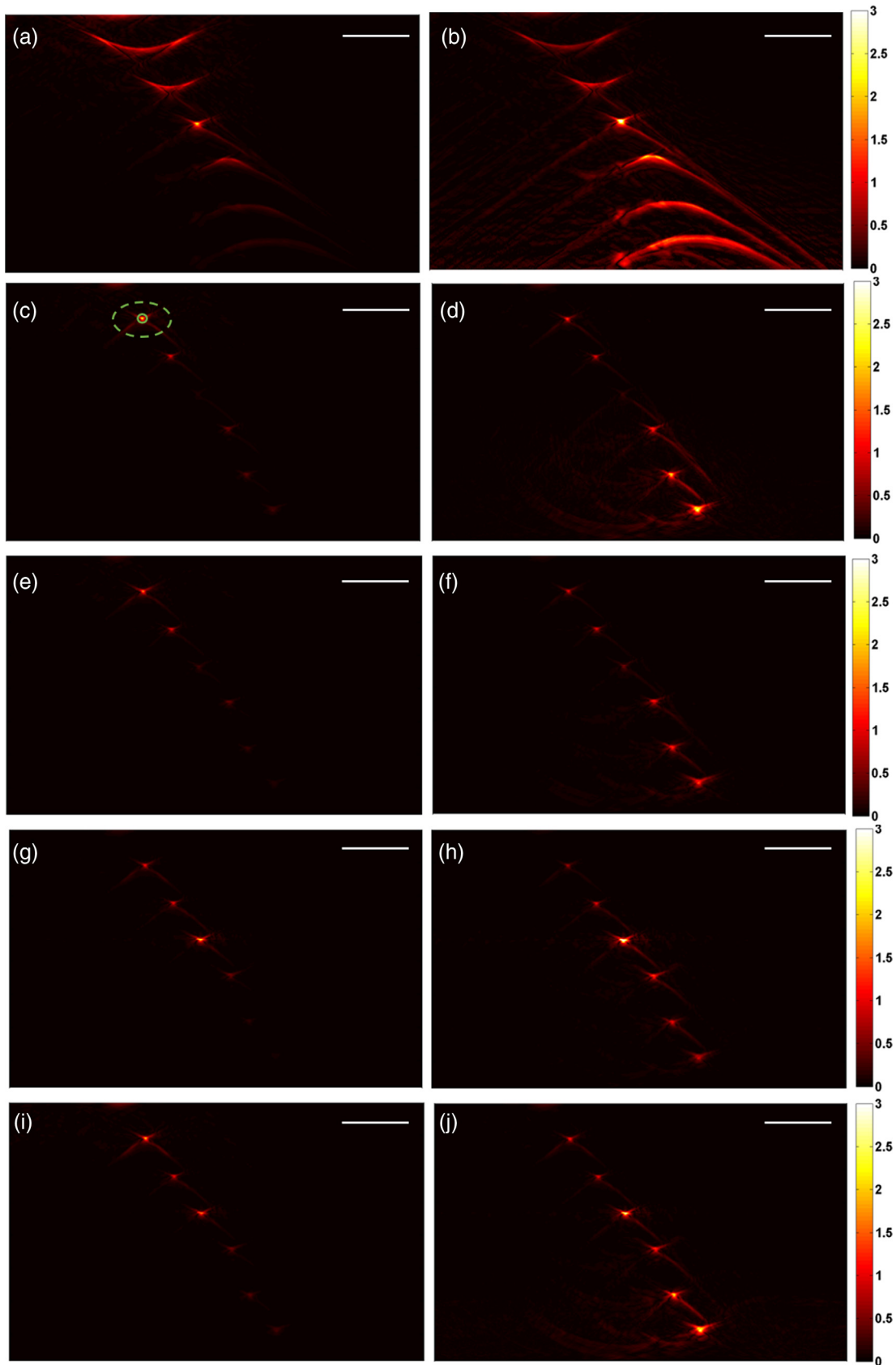


**Fig. 4** Two-dimensional reconstruction performed for the phantom with embedded absorbing wires: raw B-scans obtained by OA microscope (a, b); 2-D SAFT (c, d); 2-D SAFT + ASR (e, f); 2-D SAFT + DCM (g, h); 2-D SAFT + DCM + ASP (i, j) with (b, d, f, h, j) and without (a, c, e, g, i) fluence compensation. All bars are 1 mm. Solid and dashed green ellipses represent integration areas  $\sigma$  and  $\Sigma$  in Eq. (4), respectively.

(red line), which provides the exponential fluence decay<sup>14</sup>, and  $z_f = 1.7$  mm [Fig. 3(b) (blue line)].

The result of the fluence compensation depends on the chosen optical properties of the medium. To evaluate the effect of optical properties variations in the compensated image quality, we performed Monte Carlo simulations for 50% variations of  $\mu_a$  and  $\mu_s$  above and below the basic phantom values employed for reconstruction. The considered sets of input optical parameters are shown in Table 2: the basic optical parameters reconstructed from spectrophotometry measurements are shown as bold. The results of Monte Carlo simulations for phantom measurements for these optical properties sets are shown in Fig. 3(c).

### 3 Results

#### 3.1 Phantom Experiments

The developed approach was applied to OA data from the phantom consisting of Lipofundin solution with embedded absorbing wires. As it was mentioned in Sec. 2.1, the developed acoustic reconstruction approach consists of two parts: acoustic and optical reconstructions. The raw OA B-scan of phantom for focus position  $z_f = 1.7$ -mm under surface is shown in Fig. 4(a); the same image after fluence compensation is shown in Fig. 4(b). Note that for comparison all the images of the phantom are normalized to the signal intensity of the second wire. Fluence compensation allows to increase the signal level from deeper layers. Corresponding images after employment of 2-D conventional SAFT technique when the reconstructed image is calculated from the raw one in accordance with Eq. (2) are shown in Figs. 4(c) and 4(d) without and with fluence compensation, respectively. One can see that the application of the traditional SAFT approach allows to diminish the effect of distortions originating from acoustic detection while fluence compensation significantly increases signal level from large depths; however, the main drawback of traditional SAFT approach is the low signal from the focal plane of the system. Accounting for ASR has high potential in overcoming this drawback. The results of application of 2-D SAFT accounting for ASR are shown in Figs. 4(e) and 4(f), respectively. One can see a significant enhancement of the signal level from the focal plane; however, accurate account for ASR is very time-consuming (corresponding processing times are shown in Table 3).

To reduce computation time, accounting for ASR was substituted to combination of DCM determining ASR geometry shape and normalization to ASP. Application of the binary

mask [shown in Fig. 2(c)] alone resulting in accounting the contribution of the sources within angular aperture is shown in Figs. 4(g) and 4(h), respectively. This approach allows to significantly increase the signal from the focal point, however, at the expense of unbalanced signal in the out-of-focus region. To reduce this effect, accounting for ASP is used. Combination of these approaches for uncompensated and fluence-compensated images is shown in Figs. 4(i) and 4(j), respectively. The resultant image [Fig. 4(j)] demonstrates balanced signal level for superficial, in-focus, and deeper objects in combination with high spatial resolution simultaneously providing 35-fold speedup in processing time with respect to account for ASR (Table 3). Processing time can be further improved by performing SAFT reconstruction in a Fourier domain.<sup>25</sup>

To compare the efficiency of the applied methods, we calculated the image contrast by Eq. (4) [the areas  $\sigma$  and  $\Sigma$  are shown in Fig. 4(c) and equal to 0.008 and 0.44 mm<sup>2</sup>, respectively] for conventional 2-D SAFT reconstruction, for compensation of ASR, and for the proposed acceleration approach accounting for DCM and ASP. For each of the six wires located at different depths varying from 0.5 to 3.5 mm in the Z-direction, we calculated image contrast Fig. 5(a), axial [Fig. 5(b)], and lateral [Fig. 5(c)] resolutions. Accounting for ASR provides a twofold contrast increase in focus versus conventional SAFT [Fig. 5(a)]. Application of SAFT with DCM alone significantly increases contrast in the focal plane; however, leads to an unbalanced image contrast. Combination of DCM and ASP leads to smaller differences in image contrast at different depths. SAFT with DCM (black lines) and ASP (magenta lines) improves twice the axial resolution for reconstructed OA images in the focal area in comparison with conventional SAFT (blue lines) [Figs. 5(b)]. The considered approaches do not significantly affect lateral resolution calculated as the full width at half maximum of the image profile over the X-axis because the compensated acoustic distortions originating from the spherical detector shape are manifested in other directions. The obtained values of image contrast, axial and spatial resolutions of compensated OA B-scan for wires at focal point and at the depth of 3.5 mm under surface are shown in Table 3.

Application of conventional SAFT technique [Figs. 4(c) and 4(d)] provides high-contrast reconstruction of the signal from wires above and below the focus; however, signal amplitude in the focal area is reduced. This effect is clearly seen in the B-scans projection to the Z-axis [Fig. 6(a)]. The proposed approach (SAFT + DCM + ASP) allows to enhance the signals in focus while fluence compensation increases the signals from the depth [Fig. 6(b) (red line)].

**Table 3** Processing times, axial, and lateral spatial resolutions for different SAFT modifications applied to compensated OA B-scan of the phantom.

Method	Reconstruction time (s)	Image contrast in focus (dB)	Image contrast at 3.5 mm (dB)	Axial resolution in focus ( $\mu\text{m}$ )	Axial resolution at 3.5 mm ( $\mu\text{m}$ )	Lateral resolution in focus, ( $\mu\text{m}$ )	Lateral resolution at 3.5 mm ( $\mu\text{m}$ )
SAFT	160	3.8	8.7	98	90	80	115
SAFT + ASR	2700	6.2	8.4	68	85	75	90
SAFT + DCM	77	9.9	8.9	38	83	80	110
SAFT + DCM + ASP	80	9.8	8.8	38	83	80	105

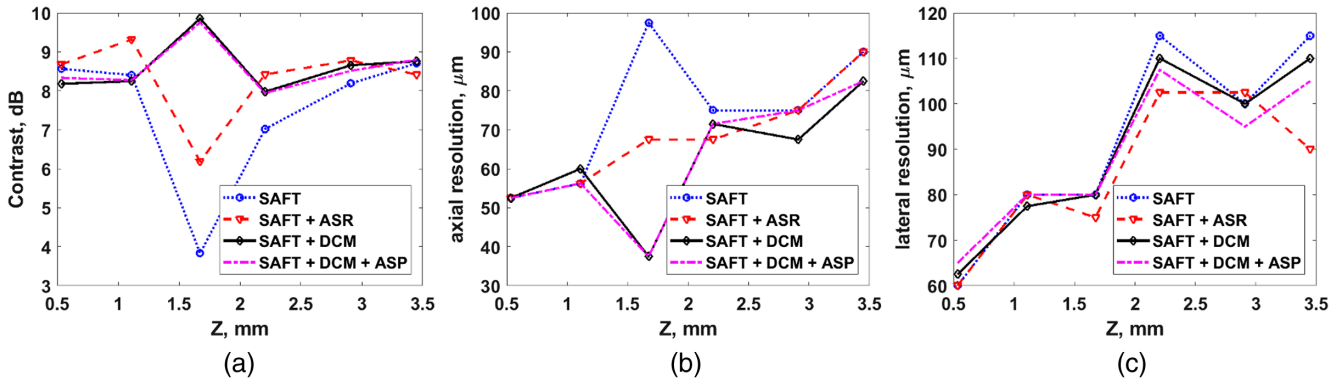


**Fig. 5** Comparison of image (a) contrast, (b) axial, and (c) lateral resolutions for OA images reconstructed by 2-D SAFT (blue lines), 2-D SAFT + ASR (red lines), 2-D SAFT + DCM (black lines), and 2-D SAFT + DCM + ASP (magenta lines) with fluence compensation.

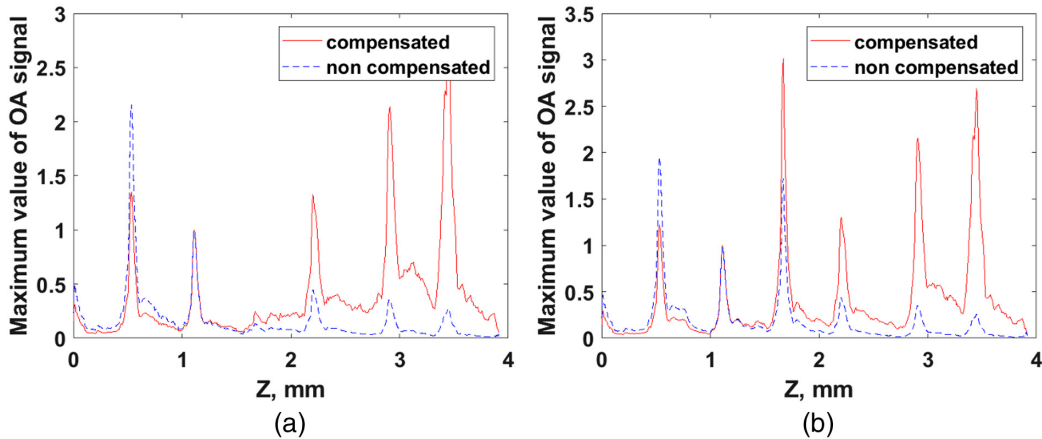


**Fig. 6** Comparison of maximum values of OA signals from absorbing wires with and without fluence compensation in projection to the Z-axis for two reconstruction methods: conventional 2-D SAFT (a) and 2-D SAFT + DCM + ASP (b).

As one can see from Fig. 4(j), the fluence compensation can enhance the contrast of deep wires compared with uncompensated image [Fig. 4(i)]; however, the effect of compensation depends on the chosen optical properties. Therefore, we performed SAFT + DCM + ASP reconstruction with Monte Carlo-simulated fluence distribution for 50% variations of  $\mu_a$  and  $\mu_s$  above and below the basic values for phantom (Table 2).

From Fig. 7, one can see that the Monte Carlo-derived fluence distribution allows to improve contrast of deep wires, even if the selected optical parameters differ from basic values; however, a strong increase of  $\mu_a$  [Fig. 7(d)] or  $\mu_s$  [Fig. 7(f)] slightly decreases the contrast of wires located close to the surface.

In contrast to Ref. 13 where the fluence distribution is considered as an exponential, we calculated it accounting for the complex illumination beam shape. To compare the results of compensation techniques, we performed reconstruction and further compensation both to exponential decay [Fig. 3(b) (red line)] and complex Monte Carlo-simulated fluence [Fig. 3(b) (blue line)]. Figure 8(b) shows the image compensated for exponential fluence distribution [Fig. 3(b) (red line)] that corresponds to the Monte Carlo modeling for  $z_f = 0$  mm.

This figure demonstrates that compensation for exponential dependence significantly improves the contrast of deep wires at depths from 2 to 3.5 mm, which are not distinguished in the uncompensated image [Fig. 8(a)]. However, such compensation significantly decreases the signal from superficial layers resulting in almost complete disappearance of the superficial wires [Fig. 8(b)] as compared with [Fig. 8(a)] in the image. Figure 8(c) shows the image compensated for Monte Carlo-derived fluence distribution calculated for corresponding focus position  $z_f = 1.7$  mm [Fig. 8(c)] proving that such compensation provides much better results as compared with compensation for exponential due to better image balance.

### 3.2 In-Vivo Experiments

The developed approach of SAFT with account for DCM and ASP and fluence compensation was applied to OA images of human palm *in vivo*. First, to each B-scan from 3-D matrix (which corresponds to a fixed position in the Y-direction), we employed 2-D SAFT reconstruction accounting for DCM and normalizing to ASP. Second, to each A-scan from OA 3-D data, we applied Monte Carlo-derived fluence compensation for focus position  $z_f = 1.5$  mm [Fig. 3(a) (blue line)]. 3-D

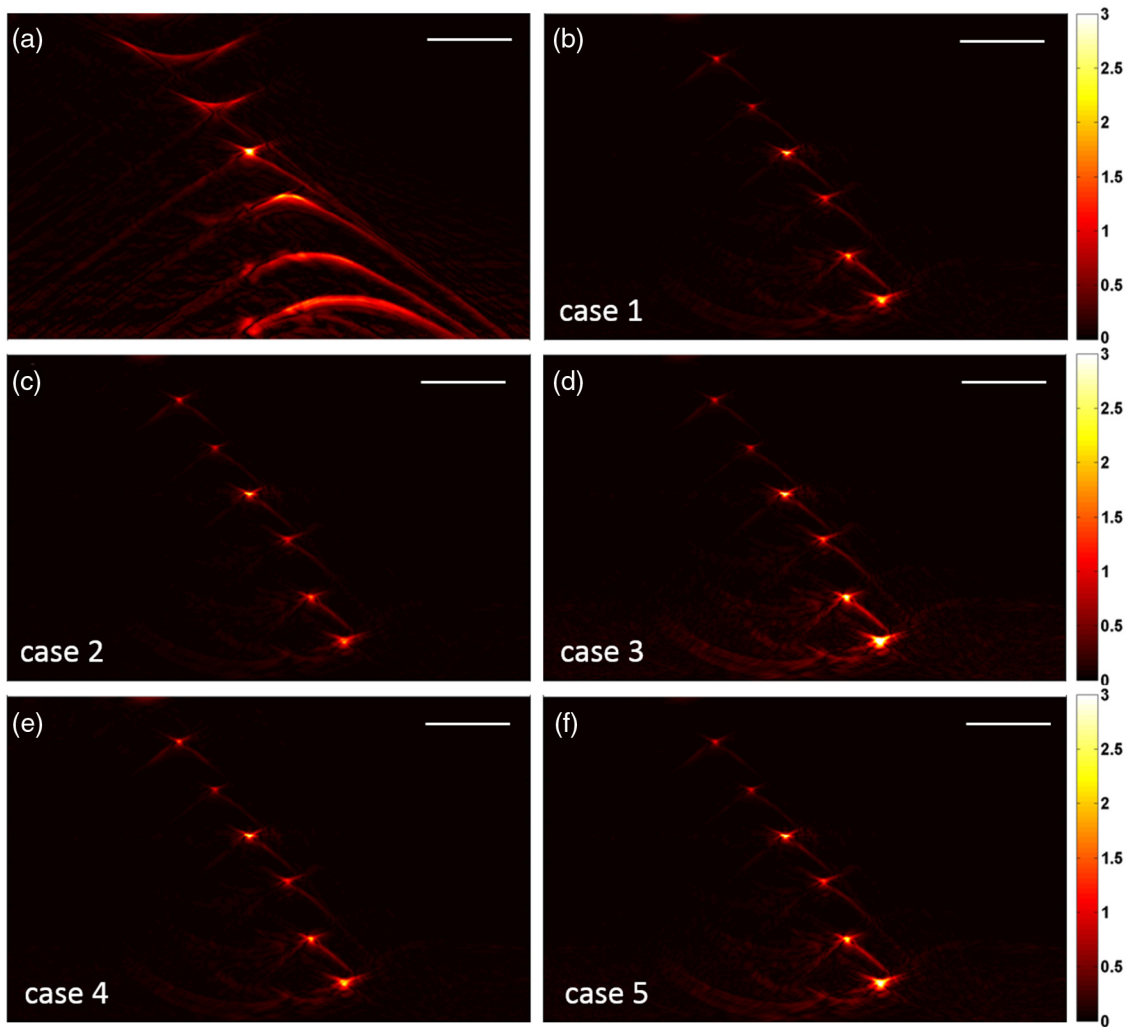


**Fig. 7** B-scans of the phantom with embedded absorbing wires before (a) and after 2-D SAFT + DCM + ASP reconstruction with compensation for Monte Carlo-simulated fluence distribution for different input optical parameters (b–f) shown in Table 2. All bars are 1 mm.

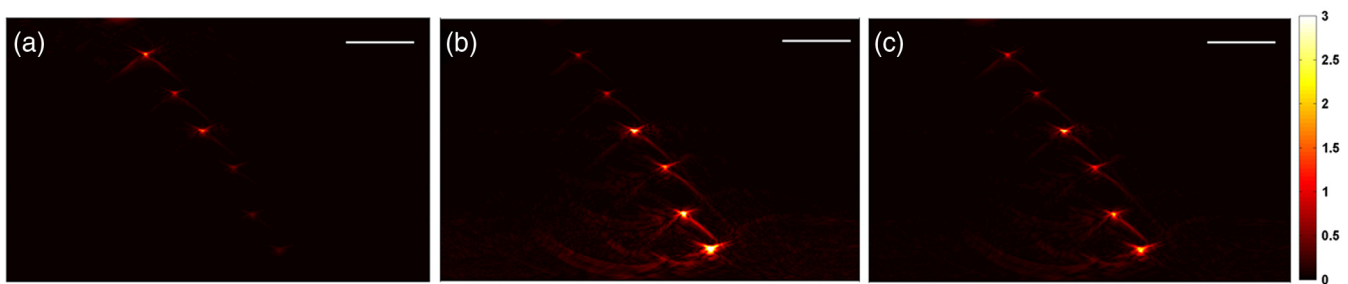


**Fig. 8** Reconstructed B-scans by 2-D SAFT + DCM + ASP algorithm without (a) and with fluence compensation for exponential fluence distribution (b), and fluence distribution accounting for complex illumination geometry (c). All bars are 1 mm.

reconstructed image was formed from the set of reconstructed *B*-scans as full 3-D reconstruction approach leads to artifacts originating from the object motion during scanning.

In Fig. 9, one can see two raw [Figs. 9(a) and 9(e)] and fluence-compensated [Figs. 9(b) and 9(f)] *B*-scans with corresponding SAFT + DCM + ASP reconstructed [Figs. 9(c), 9(d), 9(g), and 9(h)] *B*-scans for two different *Y*-positions

(dashed and solid frames, respectively) without [Figs. 9(c) and 9(g)] and with [Figs. 9(d) and 9(h)] fluence compensation.

Figure 10 shows raw depth-color-encoded *en face* OA images of human palm vasculature, built in Fiji,<sup>26</sup> with  $z_f = 1.5$  mm obtained by the AR-PAM system without [Fig. 10(a)] and with [Fig. 10(b)] fluence compensation together with reconstructed (SAFT + DCM + ASP-processed) images without

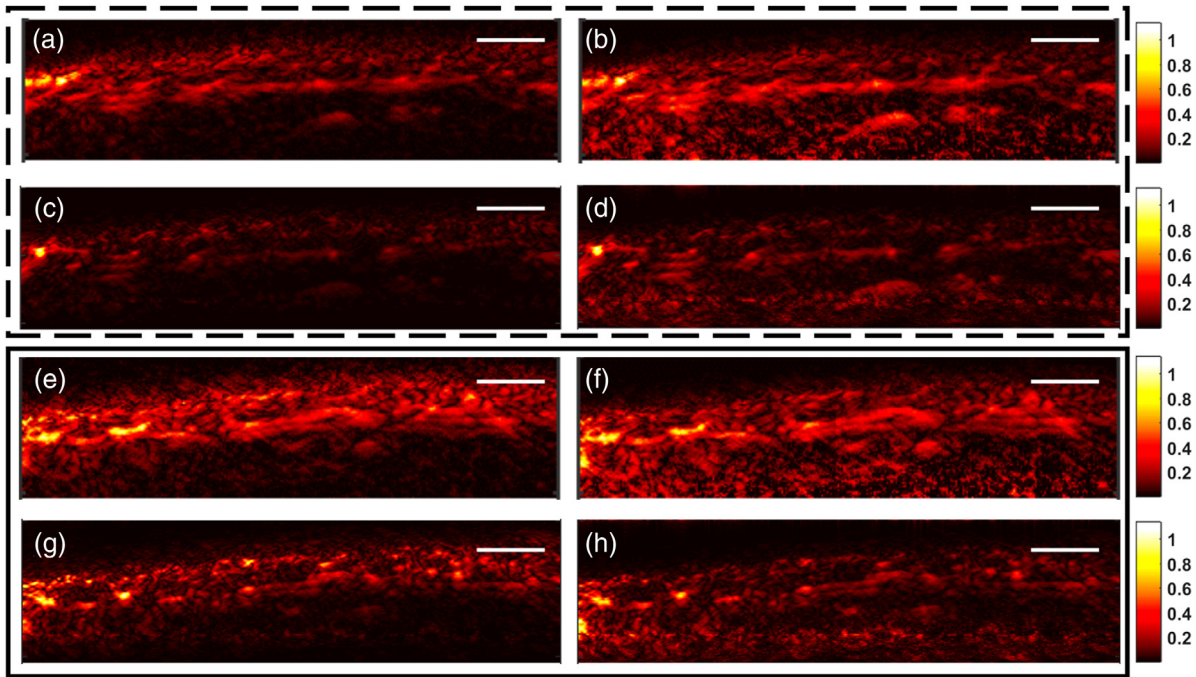


**Fig. 9** Two-dimensional reconstruction performed for OA B-scans of human palm vasculature: raw B-scans of human palm obtained by OA microscope (a, b, e, and f); results of 2-D SAFT + DCM + ASP (reconstruction time 41 s) (c, d, g, and h) with (right column) and without (left column) fluence compensation. All bars are 1 mm.

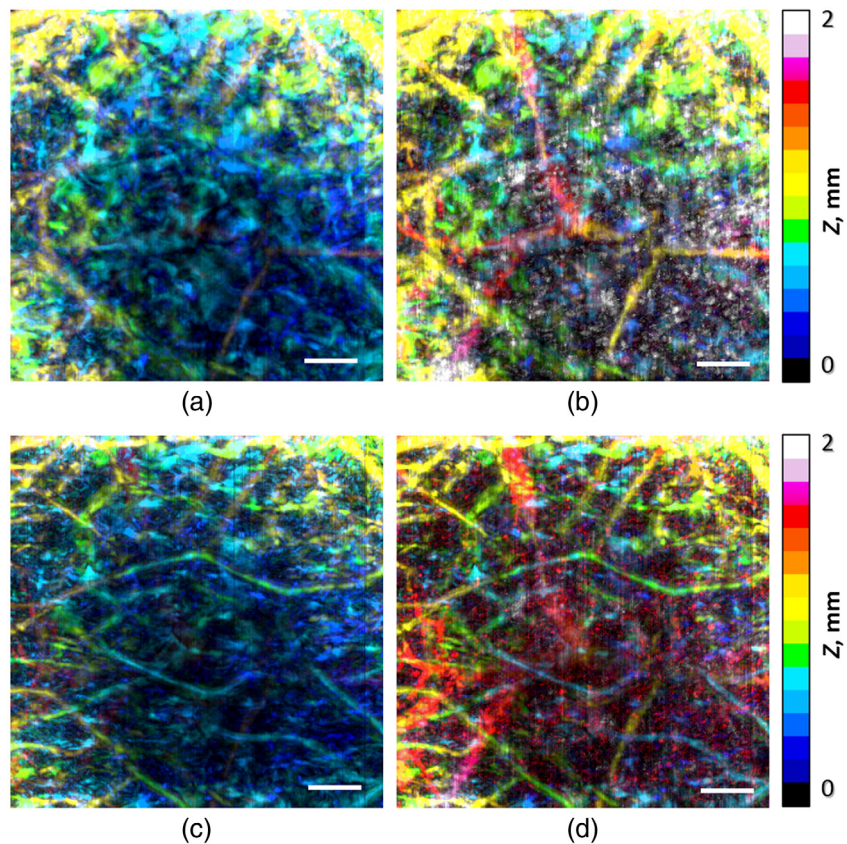


**Fig. 10** Depth-color-encoded AR-PAM images of human palm vasculature with focus position at the depth of 1.5 mm: raw OA 3-D image (a, b) and reconstructed OA 3-D image by 2-D SAFT + DCM + ASP (Video 1) uncompensated (a, c), and compensated for Monte Carlo-simulated AR-PAM fluence distribution (b, d). All bars are 1 mm (Video 1, MPEG, 7.1 MB [URL: <https://doi.org/10.1117/1.JBO.23.9.091414.1>]).

[Fig. 10(c)] and with [Fig. 10(d)] fluence compensation. The images prove enhancement of OA signals from deeper layers.

## 4 Discussion

The proposed combination of fluence compensation and SAFT + DCM + ASP approach accounting for the ASR demonstrated an improved performance as compared with the conventional SAFT used in AR-PAM experimental data processing.

Traditional SAFT reduces the artifacts that originate from acoustic detection leading; however, leads to low signal from the focal plane of the system. SAFT + ASR provides a significant enhancement of the signal level from the focal plane, whereas fluence compensation increases signal level from large depths.

Accurate account for ASR is rather time-consuming; however, the reconstruction time can be decreased by applying different optimization techniques. Instead of time-consuming reconstruction by SAFT + ASR, we implemented both 2-D DCM corresponding to the geometrical shape of ASR angular aperture and in-depth normalization in accordance with 1-D ASP. Both of these characteristics were derived from the simulated ASR.

Reduced quality of ASR reconstruction (Table 3) as compared with simplified SAFT + DCM + ASP approach can be explained by the fact that the ASR was constructed as a maximum of detector impulse response at a given point, and did not account for the shape of the temporal impulse response. Indeed, when a source is placed outside of DOF, the signal shape strongly changes<sup>27</sup> [Fig. 2(a)]. Accounting for the differences in temporal profiles of the detector impulse response can be performed through additional procedures, such as deconvolution.<sup>11</sup>

Accounting for the detector temporal impulse responses can also provide further improvement of the SAFT + DCM + ASP technique. Depth-dependent impulse response of the detector could be responsible for decreased quality of acoustic reconstruction for phantom experiment (Fig. 4) as it was performed at diagnostic depths exceeding DOF [Fig. 2(a)]. Therefore, deconvolution-based procedures equalizing the detector's impulse response for various depths would be the most helpful for phantom study. As *in-vivo* studies were performed within DOF, accounting for finite impulse response could provide rather minor improvements in *in-vivo* OA images.

The resulting SAFT + DCM + ASP procedure demonstrated 35-fold speedup in processing time with respect to SAFT + ASR while preserving the balanced signal level for superficial, in-focus, and deeper elements. Along with the decrease in the computation time, the proposed method provides twofold improvement in axial resolution for the reconstructed phantom images in the focal area in comparison with conventional SAFT. Similar trend was proposed by another group when the SAFT technique of accounting for spatial impulse response weighting mask<sup>10</sup> was further substituted with two binary masks of spatial impulse response and fluence distribution.<sup>13</sup> However, in Ref. 13, the fluence distribution is considered as an exponential dependence, while we calculated it accounting for the complex illumination beam shape.

In phantom experiment, we demonstrated that compensation for exponential dependence significantly improves images ensuring higher signal from deep embedded wires that are not distinguished in uncompensated images. However, exponential compensation significantly decreases the signal from

superficial layers resulting in almost complete disappearance of the superficial wires, whereas compensation to Monte Carlo-derived fluence distribution provides much better results as compared to compensation for exponential dependence.

Since the optical properties even of the phantom are known with inaccuracy, further tuning the optical properties can improve the results of the proposed approach. Nevertheless, the compensation works well enough and depend slightly on the employed values of the optical properties, thus such a compensation can be efficiently performed, even though the optical properties are known only approximately.

## 5 Conclusions

Optimal performance of AR-PAM requires further processing of the obtained raw images to eliminate distortions originating from in-depth fluence attenuation and acoustic detection artifacts. We employed a combination of SAFT with account for probing optical fluence distribution within medium and spatial antenna sensitivities. Fluence compensation for each A-scan was based on 3-D Monte Carlo simulation accounting for actual complex geometry of the OA illumination system and optical properties of studied phantom and *in-vivo* objects. ASR matrix was derived from numerical solution of acoustic wave equation; however, its employment in direct form appeared to be very time-consuming. To reduce computational time, an acceleration approach was proposed consisting in substitution of ASR with detection cone mask and normalization to 1-D ASP. Application of both reconstruction and fluence compensation allowed to enhance OA image quality.

### Disclosures

The authors have no conflicts of interests.

### Acknowledgments

The work was supported by the Russian Science Foundation, Project No. 14-15-00709-II.

### References

1. M.-L. Li et al., "Improved in vivo photoacoustic microscopy based on a virtual-detector concept," *Opt. Lett.* **31**(4), 474–476 (2006).
2. M. Omar et al., "Optical imaging of post-embryonic zebrafish using multi orientation raster scan optoacoustic mesoscopy," *Light: Sci. Appl.* **6**(1), e16186 (2017).
3. L. Ding, X. L. Dean Ben, and D. Razansky, "Efficient three-dimensional model-based reconstruction scheme for arbitrary optoacoustic acquisition geometries," *IEEE Trans. Med. Imaging* **36**, 1858–1867 (2017).
4. A. Ramalli et al., "High dynamic range ultrasound imaging with real-time filtered-delay multiply and sum beamforming," in *IEEE Int. Ultrasonics Symp. (IUS)*, pp. 1–4 (2017).
5. G. Matrone et al., "Depth-of-field enhancement in filtered-delay multiply and sum beamformed images using synthetic aperture focusing," *Ultrasonics* **75**, 216–225 (2017).
6. J. F. Synnevag, A. Austeng, and S. Holm, "Adaptive beamforming applied to medical ultrasound imaging," *IEEE Trans. Ultrason. Ferroelectr. Freq. Control* **54**(8), 1606–1613 (2007).
7. C.-K. Liao, M.-L. Li, and P.-C. Li, "Optoacoustic imaging with synthetic aperture focusing and coherence weighting," *Opt. Lett.* **29**(21), 2506–2508 (2004).
8. Z. Deng et al., "Two-dimensional synthetic-aperture focusing technique in photoacoustic microscopy," *J. Appl. Phys.* **109**(10), 104701 (2011).
9. Z. Deng et al., "Adaptive synthetic-aperture focusing technique for microvasculature imaging using photoacoustic microscopy," *Opt. Express* **20**(7), 7555–7563 (2012).

10. J. Turner et al., "Improved optoacoustic microscopy through three-dimensional spatial impulse response synthetic aperture focusing technique," *Opt. Lett.* **39**(12), 3390–3393 (2014).
11. D. Cai et al., "Photoacoustic microscopy in vivo using synthetic-aperture focusing technique combined with three-dimensional deconvolution," *Opt. Express* **25**(2), 1421–1434 (2017).
12. M. Schwarz et al., "Motion correction in optoacoustic mesoscopy," *Sci. Rep.* **7**(1), 10386 (2017).
13. J. Turner et al., "Universal weighted synthetic aperture focusing technique (W-SAFT) for scanning optoacoustic microscopy," *Optica* **4**(7), 770–778 (2017).
14. M. Kirillin et al., "Fluence compensation in raster-scan optoacoustic angiography," *Photoacoustics* **8**, 59–67 (2017).
15. J. Park et al., "Delay-multiply-and-sum-based synthetic aperture focusing in photoacoustic microscopy," *J. Biomed. Opt.* **21**(3), 036010 (2016).
16. M. Mozaffarzadeh et al., "Double stage delay multiply and sum beamforming algorithm: application to linear-array photoacoustic imaging," *IEEE Trans. Biomed. Eng.* **65**, 31–42 (2017).
17. T. Khokhlova, I. Pelivanov, and A. Karabutov, "Optoacoustic tomography utilizing focused transducers: the resolution study," *Appl. Phys. Lett.* **92**(2), 024105 (2008).
18. L. Zhao et al., "Optical fluence compensation for handheld photoacoustic probe: an in vivo human study case," *J. Innovative Opt. Health Sci.* **10**(04), 1740002 (2017).
19. V. Perekatova, I. Fiks, and P. Subochev, "Image correction in optoacoustic microscopy. Numerical simulation," *Radiophys. Quantum Electron.* **57**(1), 67–79 (2014).
20. B. E. Treeby and B. T. Cox, "k-Wave: MATLAB toolbox for the simulation and reconstruction of photoacoustic wave fields," *J. Biomed. Opt.* **15**(2), 021314 (2010).
21. P. Subochev, "Cost-effective imaging of optoacoustic pressure, ultrasonic scattering, and optical diffuse reflectance with improved resolution and speed," *Opt. Lett.* **41**(5), 1006 (2016).
22. P. Subochev et al., "Simultaneous in vivo imaging of diffuse optical reflectance, optoacoustic pressure, and ultrasonic scattering," *Biomed. Opt. Express* **7**(10), 3951–3957 (2016).
23. A. Bashkatov et al., "Optical properties of human skin, subcutaneous and mucous tissues in the wavelength range from 400 to 2000 nm," *J. Phys. D: Appl. Phys.* **38**(15), 2543–2555 (2005).
24. A. N. Bashkatov, E. A. Genina, and V. V. Tuchin, "Optical properties of skin, subcutaneous, and muscle tissues: a review," *J. Innovative Opt. Health Sci.* **4**(01), 9–38 (2011).
25. M. Jaeger et al., "Fourier reconstruction in optoacoustic imaging using truncated regularized inverse k-space interpolation," *Inverse Prob.* **23**(6), S51 (2007).
26. J. Schindelin et al., "Fiji: an open-source platform for biological-image analysis," *Nat. Methods* **9**(7), 676–682 (2012).
27. H. Roitner et al., "Deblurring algorithms accounting for the finite detector size in photoacoustic tomography," *J. Biomed. Opt.* **19**(5), 056011 (2014).

**Valeriya V. Perekatova** is a junior researcher at the Laboratory of Biophotonics at the Institute of Applied Physics of the Russian Academy of Sciences (RAS). She received her master's degree in Physics in 2015 from Lobachevsky State University of Nizhny Novgorod. Her current research focuses on the developing the methods of optoacoustic imaging of biological tissues. She is a member of SPIE and ASA. She is a coauthor of 10 peer-review articles and conference proceedings related to optoacoustics.

**Mikhail Yu. Kirillin** is a senior researcher at the Laboratory of Biophotonics of Institute of Applied Physics of the Russian Academy of Sciences. He received his PhD from Moscow State University, Russia, in 2006 and his DSc (Tech) degree from the University of Oulu, Finland, in 2008. His scientific interests include biomedical imaging modalities, theoretical descriptions, and numerical simulations (in particular, Monte Carlo technique) of light transport in scattering media.

**Ilya V. Turchin** is the head of the department for radiophysics methods in medicine at the Institute of Applied Physics of RAS and is an expert in optical imaging systems design (optical diffuse imaging, fluorescence imaging, photoacoustics) and biomedical applications. He has over 10 years of experience as a primary investigator in optical imaging, photodynamic therapy, and translation of optical techniques into clinics. He has published more than 50 peer-review articles.

**Pavel V. Subochev** is the optoacoustic group leader at the Laboratory of Biophotonics, Institute of Applied Physics, RAS. He graduated from Lobachevsky State University of Nizhny Novgorod in 2006 and received his PhD in passive acoustic radiometry from the Institute of Applied Physics of Russian Academy of Sciences. Since 2012, he has focused on the development of new instrumentation for optoacoustics imaging of biological tissues. He is the co-author of 30 peer-review articles and conference proceedings related to optoacoustics.